IOP Conf. Series: Journal of Physics: Conf. Series **843** (2017) 012037 doi:10.1088/1742-6596/843/1/012037

Correlation between cavitation erosion resistance and cyclic mechanical properties of different metallic materials

Corinna Kaufhold[1], Fabian Pöhl and Werner Theisen

Chair of Materials Technology, Ruhr University Bochum, 44801 Bochum, Germany

[1]Corresponding author: hardes@wtech.rub.de

Abstract. Machine components in contact with flowing fluids are especially prone to cavitation erosion, where plastic deformation and material loss occur due to the repeated implosion of cavitation bubbles in the vicinity of a solid surface. Identifying a correlation between experimentally derivable material properties and resistance against cavitation erosion could help improve the lifetime of cavitation-affected components. Cavitation erosion is a predominantly fatigue-driven phenomenon. In this investigation, we conducted nanoindentation experiments to examine cyclic micromechanical material properties in response to an increasing number of cycles. The experiments were performed on pure iron and different steel grades, i.e., austenitic stainless CrMnCN steels, interstitially alloyed with carbon and nitrogen. We confirmed the view, also proposed in literature, that indentation hardness is inappropriate for ordering the investigated materials by incubation period or maximum erosion rate. We found that the percentage increase of nanoindentation contact stiffness, after an increasing number of cycles, is a promising indicator in terms of the overall ranking of cavitation erosion resistance among the considered materials. Although a single cavitation impact is associated with a significantly higher strain rate than nanoindentation experiments, it is shown that the plastically deformed area around each indent exhibits indications of deformation, such as the formation of slip lines that are also observable after cavitation-induced impacts.

1. Introduction

Cavitation erosion is a specific form of wear that reduces the quality and lifespan of engineering units and components employed in streaming liquids, e.g., marine propellers or hydraulic machinery. The implosion of a cavitation bubble near a solid structure triggers a succession of hydrodynamic events, including a wall-directed 'liquid-jet' and the subsequent emergence of shockwaves, mechanically impacting the solid surface [1]. The repeated implosion of cavitation bubbles leads to surface spallation and material fatigue [2]. While ductile materials deform plastically before material is removed, brittle materials show less plastic deformation but form fatigue cracks instead [2]. Feller and Kharazzi [3] relate a material's ability to resist cavitation erosion to a number of influencing factors: binding and stacking fault energy, crystal structure and corrosion resistance. One decisive factor is a material's deformation and transformation ability [3], elsewhere described as the materials' capacity to absorb energy [4].

Various prior investigations have discussed the correlation between material properties and resistance against cavitation erosion [3, 5–10]. Important indicators of cavitation erosion resistance include the incubation period (IP) and the maximum erosion rate (MER). Material hardness is also a widely discussed material property in this context [5–8, 10]. Richman and McNaughton [5], working

with cavitation erosion data from various researchers, found no correlation between incubation time and Vickers hardness. They attribute the lack of correlation between statically measured material properties and cavitation erosion resistance to cyclic strain hardening [5]. They identify convincing correlations between material removal rates and cyclically obtained material properties based on cyclic stress strain-curves from different authors [5].
Hattori et al. [11] developed a material database and identified a correlation between hardness and cavitation erosion resistance for carbon steels. Some stainless steels undergo considerable work-hardening, making them an exception to this tendency [11]. They ultimately found a good correlation between the cavitation erosion resistance and material hardness of stainless steels by correcting the hardness values using a material factor, taking work-hardening into account [11].

The current investigation focuses on CrMnCN steels. In these steels, the expensive alloying element nickel is replaced by manganese, which additionally enhances nitrogen solubility and thus allows production under ambient pressure [12]. The combined alloying of C and N improves yield strength, fracture strength and tensile strength [12]. The hardness and degree of work-hardening are likewise increased compared to CrNi austenites [12]. Niederhofer et al. [8] showed that the cavitation erosion resistance of CrMnCN steels is greatly enhanced compared to conventionally alloyed austenitic steel grades. Among their investigated materials, they were unable to identify a correlation between statically determined indentation hardness, H_i, and cavitation erosion resistance, determined by means of an ultrasonic horn according to ASTM G-32. However, nanoindentation was determined to be a more promising approach to correlate the mechanical properties of CN steels with cavitation erosion resistance than tensile experiments on the macroscale [8].

In this study, cyclic nanoindentation experiments were performed to find a possible correlation between mechanical properties of different metallic materials, cyclically determined on the microscale, and the ranking of these materials in terms of cavitation erosion resistance. The following questions are addressed:

- Is cyclic contact stiffness a suitable indicator for ranking the investigated materials in terms of cavitation erosion resistance?
- Does the surface pile-up in the periphery of the residual indentation imprint, after exposure to an increasing number of loading cycles, provide information about resistance against cavitation erosion?
- Does cyclic nanoindentation induce microstructural changes that are comparable to the surface indications occurring in the first stages of cavitation erosion?

2. Materials and Methods

2.1. Investigated materials and sample preparation

Pure iron, austenitic stainless steel X2CrNiMo17-12-2 (1.4404), hardened carbon steel C45, and two different grades of austenitic stainless CrMnCN steels are examined. The steels CN0.96 and CN1.07 are named after their total carbon and nitrogen content. Table 1 details the chemical composition of the investigated materials, except for pure iron, measured via spark spectroscopy. The relevant heat treatment parameters are given in Table 2.

Table 1. Chemical composition of the investigated steels in wt%.

Alloy	C	N	Cr	Mn	Mo	Ni	Si	P+S
C45	0.437		0.052	0.761	0.014	0.068	0.245	0.084
1.4404	0.011		16.59	1.592	1.913	9.940	0.381	0.064
CN0.96	0.340	0.610	18.20	18.90	0.060	0.340	0.300	
CN1.07	0.490	0.580	18.80	18.80	0.070	0.400	0.430	

Table 2. Heat treatment parameters of the investigated materials.

Alloy	Condition	Heat treatment	Temperature in °C	Time in min.
C45	As cast	Quench hardened	860	20
1.4404	As cast	Solution annealed	1070	30
CN0.96	Hot worked	Solution annealed	1100	30
CN1.07	Hot worked	Solution annealed	1175	30

In both tables, the values of CN0.96 and CN1.07 are adapted from a previous publication [8]. All austenitic steel grades were solution annealed; however, 1.4404 was quenched in oil, while the CN steels were quenched in water, due to their increased tendency to form carbide or nitride precipitates at lower cooling rates [8, 12]. All samples were mechanically grinded, polished, and finally treated with oxide polishing suspension.

2.2. Cyclic indentation testing

Micromechanical tests were performed with a nanoindentation test device (Nanomechanics, iMicro) using a Berkovich diamond tip. One approach to cyclic indentation testing is a multistep method in which multiple test cycles are applied under an increasing load, i.e., to measure the mechanical properties at different depths [13]. Alternatively, cyclic unloading and loading is performed by keeping the maximum load at the same level for each loading cycle [14]. Figure 1 shows the test method used in this study. Force-controlled experiments with a cyclically applied maximum load of 1000 mN are performed. The maximum load was kept in place for one second and fully removed after three seconds at exactly the same surface position. The corresponding load-time evolution of the applied method is schematically outlined in Figure 1.

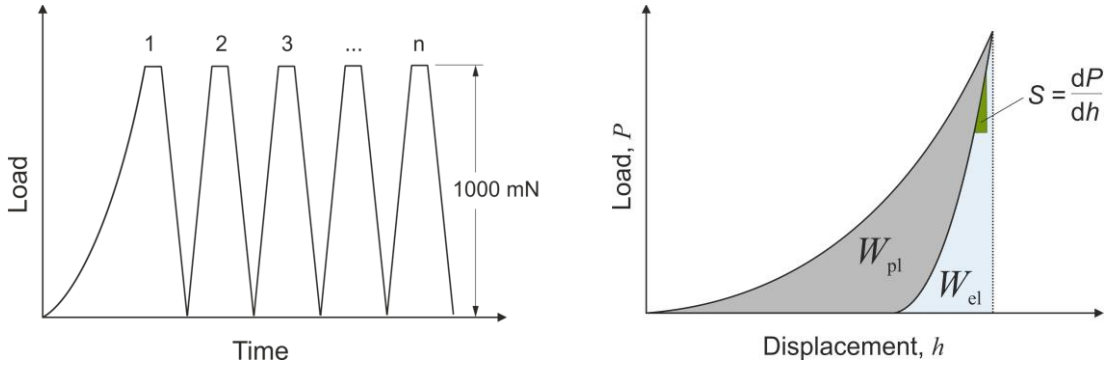

Figure 1. Schematic overview of the cyclic load-time development of the nanoindentation method (left). Simplified illustration (cf. [15]) of a load-displacement curve including the indentation stiffness, S_i, elevated using the method by Oliver and Pharr [15, 16] (right).

In each cycle, the indentation tip penetrates the previously induced indentation imprint and thus reloads the predeformed material surface. The stiffness of the indentation contact, referred to as 'indentation stiffness,' S_i, such as the indentation hardness H_i, is automatically evaluated based on the measured load-displacement curves using the method by Oliver and Pharr [16]. As illustrated in Figure 1, S_i is defined as the slope of the upper part of the unloading curve during the unloading stage under the assumption that only elastic displacements are recovered during unloading. To determine the average percentage increase in indentation stiffness after a certain number of cycles, five indentation experiments up to 250 cycles were performed. The indentation imprints were located at different positions on the sample to average the mechanical properties from differently oriented grains. The static indentation hardness and

stiffness were averaged from nine different indentation locations. The induced strain rate was set at 0.2 %/s. Poisson's ratio was defined as 0.3 for all investigated materials.

2.3. Scanning electron microscopy and atomic force microscopy

The nanoindentation experiments were performed *ex situ* and the remaining indetation imprints were subsequently analyzed with a scanning electron microscope (SEM, Tescan Mira) using a working distance of 11.09 mm, an acceleration current of 20 kV, and a magnification of 3.5 kx. To analyze the resulting surface deformation depending on an increasing number of indentation cycles, the indentation experiments were stopped after a certain number of cycles to remove the sample and to install it within the optical devices. Due to experimental restrictions, the subsequent indentation experiments were restarted from a different sample position. This only affected the indentation imprints used for the optical analysis.

The three-dimensional measurement of the indent, including the adjacent surface area, was achieved using atomic force microscopy (AFM, Bruker Nanos). The contact operation mode was used, with a scanning velocity of approx. 40 µm/s. The AFM images were analyzed using the software Gwyddion. The surface topography of the peripheral indentation area was examined along three paths. As shown in Figure 2, paths 1, 2, and 3 traverse the indent from each triangle corner to the middle of the opposite side. The resulting height profile is schematically indicated with the help of the additional image in the upper right corner of the figure. The resulting graphs are mathematically averaged and subsequently shifted along the height-axis, so that the first recorded point of each graph is set as zero level. The graphs are finally transferred along the abscissa, so the height maxima overlap at the same *x*-position.

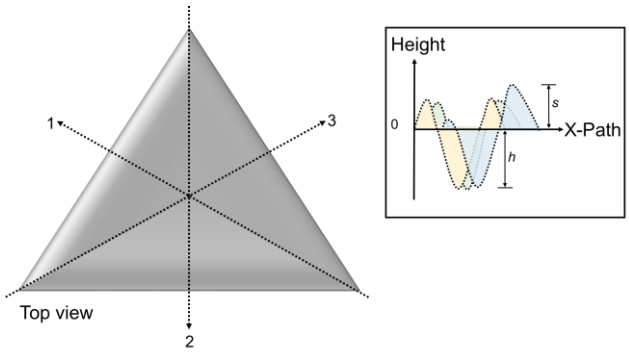

Figure 2. Schematic overview of the positions of the height profile paths traversing the surface indent, accounting for the evaluation of the average pile-up behavior of the considered materials.

To evaluate the quantitative amount of plastic deformation in response to cyclic nanoindentation, we calculated the ratio *s/h*. The height of the piled-up material around the residual indentation imprint is thereby described by *s*, while *h* represents the indentation depth (Figure 2).

3. Results and discussion

Based on cavitation erosion data adapted both from a previous investigation [8] and from literature [3, 5, 11], Table 3 shows a ranking of cavitation erosion resistance between the investigated materials.

It is known from literature that pure iron is less resistant to cavitation erosion than austenitic stainless steels in terms of incubation time and cavitation erosion rate [3]. The cavitation erosion rate is much more pronounced for iron than for all other steel grades investigated in [3]. Due to its high erosion rate and its incubation period of about 100 minutes [3], iron has the lowest cavitation erosion resistance of the investigated materials (see Table 3).

As shown in [8], CN steels exhibit enhanced cavitation erosion resistance compared to conventionally alloyed austenitic steels. Whereas the stainless austenitic steel 1.4301, investigated in [4], has an incubation period of about 152 minutes, CN steels exhibit incubation periods of 30 to 35

hours and 15 times lower erosion rates [4, 8]. CN steels are therefore the most resistant against cavitation erosion of the materials in Table 3.

In spite of their high hardness, very brittle materials show a low cavitation erosion resistance [17]. Quenched C45, in the not-annealed state, was chosen for the cyclic nanoindentation experiments, due to its brittle martensitic microstructure. As the cavitation erosion experiments of a non-stainless martensitic steel might be overshadowed by corrosion influences, stainless martensitic steels are taken as reference material in Table 3. Hattori and Ishikura [11], examining the correlation between cavitation erosion resistance and hardness, showed that austenitic stainless steels exhibit up to twice as much cavitation erosion resistance as carbon steels of the same hardness. All other investigated stainless steels, with no pearlitic content, exhibit lower cavitation erosion resistance in this case. In Table 3 stainless martensitic steel and hence C45 is ranked below the austenitic steels. Further details are discussed later.

Table 3. Investigated materials in decreasing order of cavitation erosion resistance.

Material
CrMnCN-steels
1.4404
Stl. Martensitic steel
Fe

3.1. Mechanical properties derived from cyclic nanoindentation

The indentation hardness, H_i, was derived from static nanoindentation experiments. Figure 3 shows the averaged indentation hardness, measured on various sample positions and differently orientated grains. The martensitically hardened steel C45 is the hardest of the investigated materials, whereas pure iron is the softest. CN0.96 has a higher indentation hardness than CN1.07, which was also investigated in [8]. Figure 3 shows that the statically determined hardness values do not correspond with the ranking of the investigated materials by cavitation erosion resistance. In addition to static hardness, the static indentation stiffness, S_i, and percentage stiffness increase were examined as possible indicators to estimate the ranking of this group of materials in terms of the resistance against cavitation erosion.

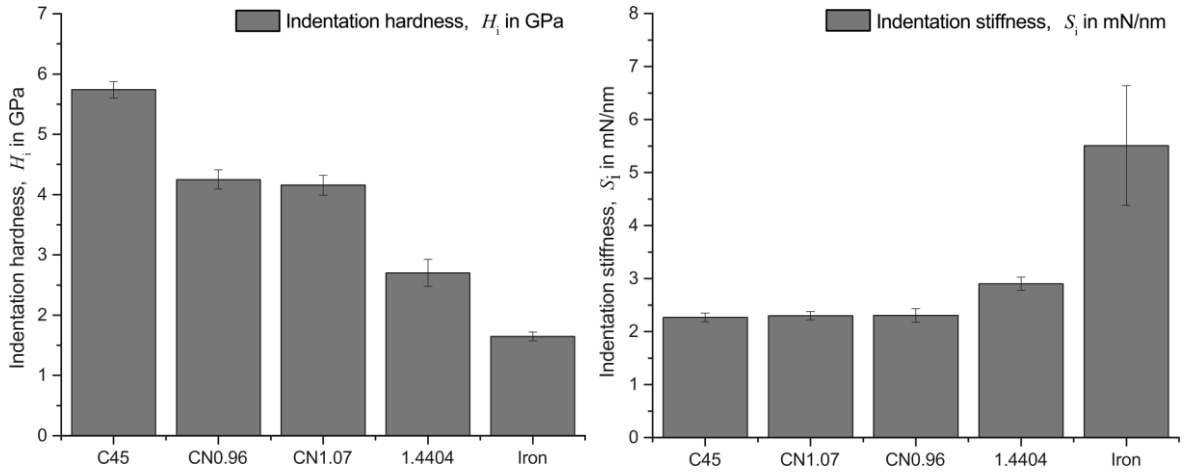

Figure 3. Indentation hardness, H_i, in GPa (left) and indentation stiffness, S_i, in mN/nm (right) averaged from nine indentations at different sample positions.

As described in Section 2.2., S_i represents the slope of the upper unloading part of the load displacement curve. A large S_i value represents a steeply sloping unloading curve and hence a large amount of plastic

deformation. According to Figure 3, CN1.07 and CN0.96 only differ slightly from each other, but differ considerably from 1.4404. Iron shows the largest static indentation stiffness, whereas C45 has the lowest. Within the group of the investigated materials, statically derived indentation stiffness seems to be just as unsuitable for determining cavitation erosion resistance as indentation hardness.
Figure 4 depicts the increase in indentation stiffness, S_i, averaged from five indentation experiments over 250 loading-unloading cycles at the same indentation imprint. An increase in indentation stiffness with an increasing number of cycles means a greater plastic share of the total deformation. CN0.96 has shown a higher hardness and a lower cavitation erosion resistance in a prior investigation [8]. It can be seen from Figure 4 that CN1.07 shows a lower S_i increase than the less cavitation-erosion-resistant CN0.96. The increased amount of work-hardening for CN1.07 is a possible explanation for the smaller S_i increase and the improved CE resistance.

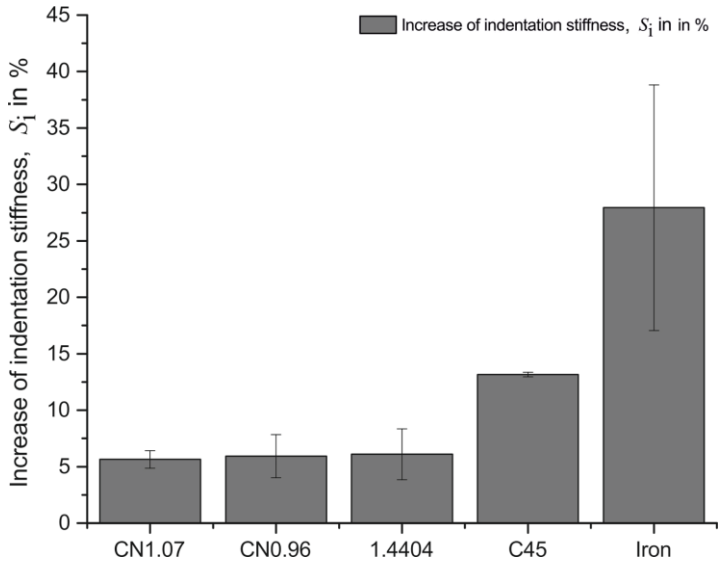

Figure 4. Increase in indentation stiffness, S_i (in %), averaged from five nanoindentation experiments over 250 loading-unloading cycles, located at different sample positions.

Compared to the other investigated austenitic steel grades, the increase in indentation stiffness exhibited by C45 and pure iron is in a completely different range. Hence, the overall ranking of the investigated materials is correct in terms of cavitation erosion resistance. However, the percentage stiffness increase shown by 1.4404 is only slightly greater compared to the CN steels, whereas its cavitation erosion resistance is many times greater, as shown in [8].
To analyze these large differences in cavitation erosion resistance in terms of mechanical properties, the indentation hardness H_i, (see Figure 3) was also taken into account. It is clear that even though the stiffness increases of the three stainless austenitic steel grades fall within a similar range, the initial hardness of the CN steels is about thirty percent greater than that of 1.4404. In this case, the stiffness increase alone is less useful for estimating the ranking of cavitation erosion resistance than the stiffness increase with respect to the indentation hardness, H_i.
Among the considered materials, iron exhibits the largest increase in indentation stiffness. This accords with its significantly lower cavitation erosion resistance compared to the other investigated materials.

3.2 Analysis of surface deformations after cyclic nanoindentation
The amount of piled-up material was examined via atomic force microscopy (AFM). Iron exhibited such extensive depth that the AFM recording was experimentally limited. Hence, iron is excluded from the following results. Figure 5 shows the averaged depth, h, of the remaining indentation imprints and the

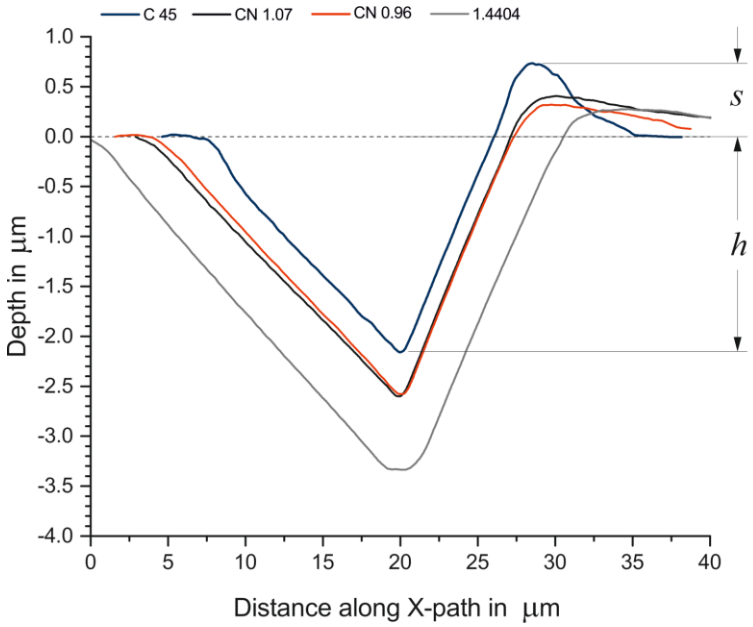

Figure 5. Averaged depth of the remaining indentation imprints and height of the piled-up material in µm, relative to the undeformed surface of the investigated materials, after 250 loading-unloading cycles.

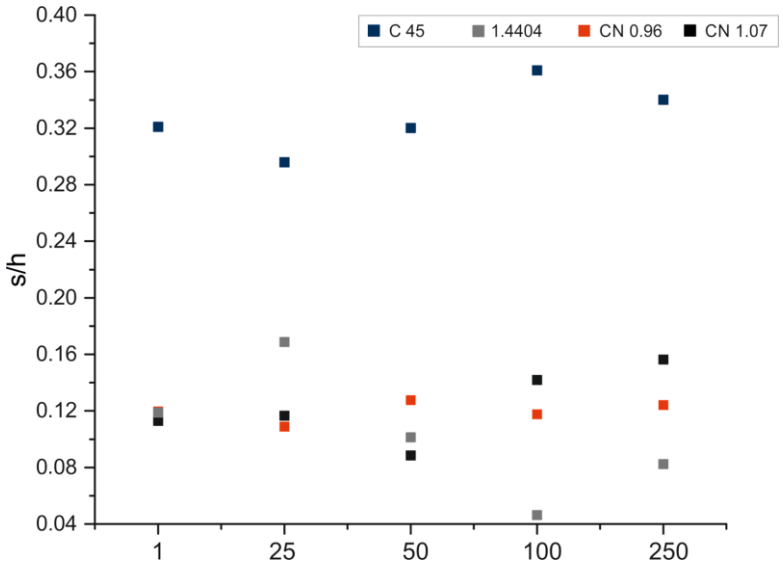

Figure 6. Ratio of pile-up, *s*, and maximum indentation depth, *h*, measured via atomic force microscopy.

amount of piled-up material, *s*, in the periphery of the penetrated surface after 250 cycles. C45 has the smallest indentation depth by a significant margin, and also the highest amount of pile-up.
Figure 6 provides an overview of the calculated *s*/*h* ratios determined from the resulting indentation imprints. The results are shown after 1, 25, 50, 100, and 250 cycles, after which the experiment was stopped to perform the optical experiments, as explained above. The investigated austenitic steels exhibit

a significantly lower *s/h* ratio overall compared to the martensitically hardened C45. Pile-up or sink-in depends on several influencing factors, including work-hardening behavior [18–20].
Yuan et al. determined, based on data by different authors (e.g. [18]), that materials with very low strain hardening coefficients show considerably larger *s/h* ratios than materials with large strain hardening coefficients. This is in approximate accordance with the differences between martensitic C45 and the austenitic steel grades depicted in Figure 5. The investigated austenitic steels reach significantly smaller *s/h* values than martensitic C45, presumably due to their greater work-hardening. No clear difference among the austenitic steel grades is distinguishable based on Figure 6. In addition to work-hardening behavior, the *s/h* ratio also depends on the grain orientation [21]. The strong fluctuations between the *s/h* values of the same material for the different cycles, plotted against the abscissa, clearly shown in Figure 6, might be due to differently oriented grains being penetrated in each cyclic indentation experiment, performed between the optical analyses.
Figure 7 shows the three-dimensional images of the indentation imprints of 1.4404 and C45 after 250 cycles. It is clear from the figure that the resulting imprint of 1.4404 occupies more of the evaluated surface area than C45. The outer edges of the originally triangular imprint are strongly curved for 1.4404, representative of the group of investigated austenitic steels. For 1.4404, the image indicates no clear amount of piled-up material. In contrast, C45 shows a significant amount of piled-up material on each side of the triangular imprint, whereas almost no material has piled-up in the corners. This behavior is also mentioned in [20] for investigations on quenched C45, using a sharp indenter. Pile-up occasionally occurs during nanoindentation experiments. If pile-up emerges, the true contact area is larger than predicted by the method of Oliver and Pharr [16], leading to an overestimate of the indentation hardness [15]. Hence, the hardness results for C45 are slightly overrated, due to the formation of pile-up. However, the overall tendencies described in this study are judged to be unaffected by this.

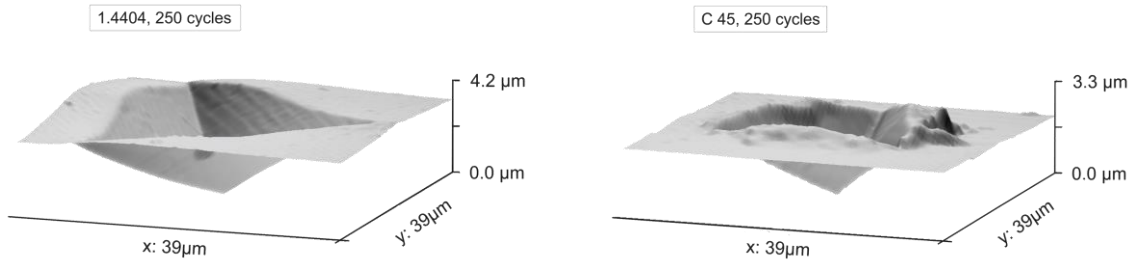

Figure 7. Three-dimensional view of the indentation imprints of 1.4404 and C45 after 250 indentation cycles.

3.3 Microstructural surface changes after cyclic nanoindentation compared to cavitation erosion
Figure 8 shows the nanoindentation imprints resulting from each 1 and 50 loading-unloading cycles. It is clear from the figure that the size of the resulting imprints increases with the number of cycles. Pronounced slip lines occur in response to the penetration of the surface with the sharp indenter. The presence of slip lines is only visible along the sides of the indentation imprint, not along the three edges. Figure 9 shows the surface of CN1.07 after exposure to cavitation erosion in an ultrasonic horn, adapted from [8]. The strong formation of slip lines is revealed. In addition, pronounced grain boundaries are apparent [8], a typical reaction of homogeneous polycrystalline materials to cavitation impacts [22].
While the formation of slip lines is detectable after both cyclic nanoindentation (Fig. 8) and cavitation erosion (Fig. 9), the material accumulation along the grain boundaries, which is relatable to a locally increased number of dislocations [22], was not apparent within the cyclic nanoindentation experiments.

Hence, the deformation mechanisms after cyclic nanoindentation experiments on up to 250 cycles can only be compared to a certain extent.

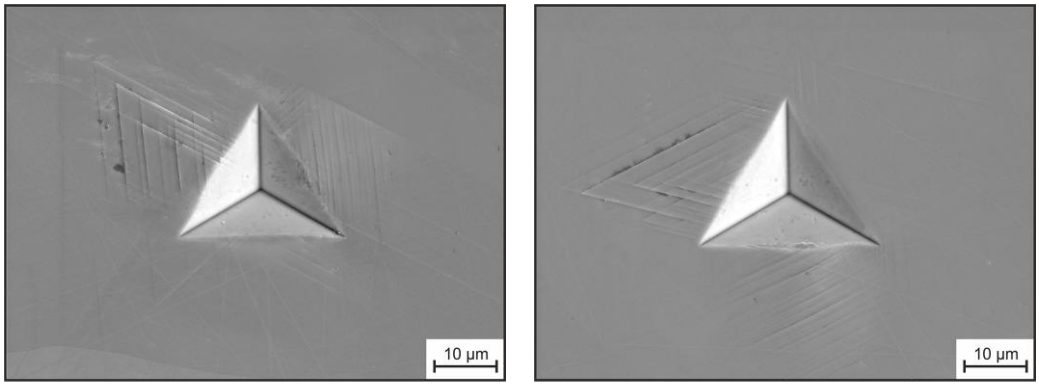

Figure 8. Resulting nanoindentation imprints in CN1.07 after 1 cycle (left) and 50 cycles (right).

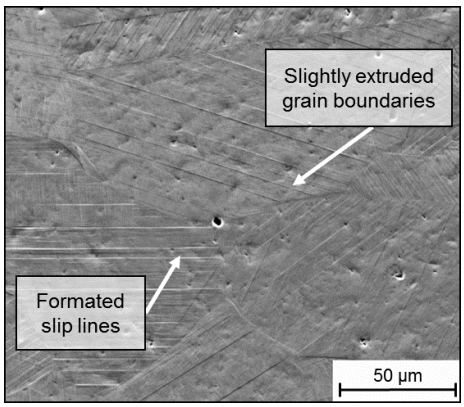

Figure 9. Electropolished surface of a CN1.07 specimen, after exposure to 2000 s of cavitation erosion in an ultrasonig horn, adapted from [8].

The deformation induced by cyclic nanoindentation experiments might vary from cavitation-induced deformations for different reasons. The material deformation resulting from cavitation-induced impacts (e.g. numerically investigated in [23]), depends on several influence factors, including the distance from the bubble center to the solid wall or the ambient pressure of the surrounding fluid [24].
In addition, the impact of cavitation bubbles is often accompanied by high strain rates in an average range of $5 * 10^3$ s^{-1} [6], which cannot be achieved during nanoindentation experiments.

4. Conclusions

The present study has shown that:

- the overall ranking of cavitation erosion resistance among the investigated materials generally agrees with the inverse increase of S_i
- the percentage differences between the S_i increases among the investigated materials do not match the differences in cavitation erosion resistance
- for CN1.07 and CN0.96, the percentage increase in S_i is a more appropriate indicator than indentation hardness
- when comparing the CN grades and 1.4404, the percentage increase in S_i seems to be more suitable as a co-factor to indentation hardness than as a standalone indicator

- even if clear differences are visible between C45 and the group of stainless austenitic steels, the *s/h* values of the three investigated austenites are out of order and do not correlate with the order of cavitation erosion resistance. The influence of the grain orientation will be further investigated
- cyclic nanoindentation leads to the formation of slip lines in the CN steels, which is also observable for cavitation erosion

5. Acknowledgements

The authors acknowledge the financial support provided by the Competence Center for Hydraulic Fluid Flow Systems at Ruhr University, Bochum (No: IV B 3-43-02/2005-WFBO-01 1Z) and especially thank U. Föckeler and O. Yilmaz for their involvement in part of the experiments.

References

[1] Philipp A and Lauterborn W 1998 Cavitation erosion by single laser-produced bubbles *J. Fluid Mech* **361** 75–116
[2] Pohl M 1990 Mikroverschleißmechanismen bei der Kavitationserosion *14. Vortragsveranstaltung des Arbeitskreises Rastermikroskopie in der Materialprüfung* ed DVM 25–36
[3] Feller H G and Kharrazi Y 1984 Cavitation erosion of metals and alloys *Wear* **93** 249–260
[4] Stella J 2004 Metallkundliche Vorgänge in der Inkubationsphase der Kavitationserosion *Ph.D. Thesis* Ruhr Universität Bochum
[5] Richman R and McNaughton W 1990 Correlation of cavitation erosion behaviour with mechanical properties of metals *Wear* **140** 63–82
[6] Kim K H, Chahine G, Franc J P and Karimi A (eds) 2014 *Advanced experimental and numerical techniques for cavitation erosion prediction* (Springer)
[7] Pohl M, Stella J and Hessing C 2003 Comparative study on CuZnAl and CuMnZnAlNiFe shape memory alloys subjected to cavitation erosion *Adv. Eng. Mater* **5** 251–256
[8] Niederhofer P and Huth S 2013 Cavitation erosion resistance of high interstitial CrMnCN austenitic stainless steels *Wear* **301** 457–466
[9] Stella J, Pohl M, Bock C and Kunze U 2014 Influence of grain orientation on the local deformation mode induced by cavitation erosion in a CuSnNi alloy *Wear* **316** 1–5
[10] Duraiselvam M, Galun R, Wesling V, Mordike B L, Reiter R and Oligmüller J 2006 Cavitation erosion resistance of AISI 420 martensitic stainless steel laser-clad with nickel aluminide intermetallic composites and matrix composites with TiC reinforcement *Surf Coat Tech* **201** 1289–1295
[11] Hattori S and Ishikura R 2010 Revision of cavitation erosion database and analysis of stainless steel data *Wear* **269** 109–116
[12] Berns H, Riedner S and Tyshchenko A I Stainless Austenitic CrMnCN Steels of Superior Strength Part I. Alloy Design and Properties *Materials Science Forum* **539-543** 4956–4961
[13] Shuman D, Costa A L M and Andrade M S 2007 Calculating the elastic modulus from nanoindentation and microindentation reload curves *Materials Characterization* **58** 380–389
[14] Nêmeček J 2009 Creep effects in nanoindentation of hydrated phases of cement pastes *Materials Characterization* **60** 1028–1034
[15] Oliver W C and Pharr G M 2004 Measurement of hardness and elastic modulus by instrumented indentation: Advances in understanding and refinements to methodology *J Mater Res* **19** 3–20
[16] Oliver W C and Pharr G M 1992 An improved technique for determing hardness and elastic modulus using load and displacement sensing indentation experiments *J Mater Res* **7** 1564–1583

[17] Gülich J F 2014 *Centrifugal Pumps* 3rd Edition (Springer Berlin Heidelberg)
[18] Taljat B and Pharr G M 2004 Development of pile-up during spherical indentation of elastic-plastic solids *Int J Solids Struct* **41** 3891–3904
[19] Yuan F, Jiang P., Xie J and Wu X 2012 Analysis of spherical indentation of materials with plastically graded surface layer *International Journal of Solids and Structures* **49** 527–536
[20] Zhu L N, Xu B S, Wang H D and Wang C B 2013 Pileup behavior in sharp nanoindentation of AISI 1045 steel *Phys Procedia* **50** 214–218
[21] Renner E, Gaillard Y, Richard F, Amiot F and Delobelle P 2016 Sensitivity of the residual topography to single crystal plasticity parameters in Berkovich nanoindentation on FCC nickel *Int J Plasticity* **77** 118–140
[22] Pohl M 1990 *Werkstoffverhalten bei Kavitation* Tagungsband der Tribologie Fachtagung der Gesellschaft für Tribologie e.V. "Verschleiß-Technik" 7/1
[23] Pöhl F, Mottyll S, Skoda R and Huth S 2015 Evaluation of cavitation-induced pressure loads applied to material surfaces by finite-element-assisted pit analysis and numerical investigation of the elasto-plastic deformation of metallic materials *Wear* **330-331** 618–628
[24] Lauer E, Hu X Y, Hickel S and Adams N A 2012 Numerical modelling and investigation of symmetric and asymmetric cavitation bubble dynamics *Comput Fluids* **69** 1–19